Effect of interfacial solute segregation on ductile fracture of Al–Cu–Sc alloys

7 authors, including:

G. Liu
Xi'an Jiaotong University
126 PUBLICATIONS **2,621** CITATIONS

SEE PROFILE

Jinyu Zhang
State Key Laboratory for Mechanical Behav…
56 PUBLICATIONS **506** CITATIONS

SEE PROFILE

Jianzhong Sun
Nanjing University of Aeronautics & Astron…
301 PUBLICATIONS **9,727** CITATIONS

SEE PROFILE

Effect of interfacial solute segregation on ductile fracture of Al–Cu–Sc alloys

B.A. Chen [a], G. Liu [a,*], R.H. Wang [b], J.Y. Zhang [a], L. Jiang [a], J.J. Song [a], J. Sun [a,*]

[a] *State Key Laboratory for Mechanical Behavior of Materials, Xi'an Jiaotong University, Xi'an 710049, China*
[b] *School of Materials Science and Engineering, Xi'an University of Technology, Xi'an 710048, China*

Abstract

Three-dimensional atom probe analysis is employed to characterize the Sc segregation at θ'/α-Al interfaces in Al–2.5 wt.% Cu–0.3 wt.% Sc alloys aged at 473, 523 and 573 K, respectively. The interfacial Sc concentration is quantitatively evaluated and the change in interfacial energy caused by Sc segregation is assessed, which is in turn correlated to yield strength and ductility of the alloys. The strongest interfacial Sc segregation is generated in the 523 K-aged alloy, resulting in an interfacial Sc concentration about 10 times greater than that in the matrix and a reduction of ~25% in interfacial energy. Experimental results show that the interfacial Sc segregation promotes θ' precipitation and enhances the strengthening response. A scaling relationship between the interfacial energy and precipitation strengthening increment is proposed to account for the most notable strengthening effect observed in the 523 K-aged alloy, which is ~2.5 times that in its Sc-free counterpart and ~1.5 times that in the 473 and 573 K-aged Al–Cu–Sc alloys. The interfacial Sc segregation, however, causes a sharp drop in the ductility when the precipitate radius is larger than ~200 nm in the 523 K-aged alloy, indicative of a transition in fracture mechanisms. The underlying fracture mechanism for the low ductility regime, revealed by in situ transmission electron microscopy tensile testing, is that interfacial decohesion occurs at the θ' precipitates ahead of crack tip and favorably aids the crack propagation. A micromechanical model is developed to rationalize the precipitate size-dependent transition in fracture mechanisms by taking into account the competition between interfacial voiding and matrix Al rupture that is tailored by interfacial Sc segregation.

© 2012 Acta Materialia Inc. Published by Elsevier Ltd. All rights reserved.

Keywords: Aluminum alloys; Solute segregation; Fracture mechanism; Interfacial decohesion; Precipitate

1. Introduction

Aluminum alloys combine high strength and light weight and are thus of utmost importance as structural materials. In particular, heat-treatable Al alloys, which are strengthened by the formation of precipitates, are used extensively in the automotive and aviation industries [1]. The binary Al–Cu system is a well-studied precipitation strengthening system because it forms the basis for a wide range of age-hardening alloys. The precipitation sequence observed on aging these alloys, supersaturated solid solution (SSSS) → Guinier–Preston (GP) zones → $\theta'' \to \theta' \to \theta$, is often used as a model system for describing the fundamentals of precipitation hardening [2].

Small additions of various alloying elements are of prime importance in modifying the precipitation/microstructure and improving the mechanical properties of Al alloys [3]. Such microalloying effects have also been applied to the Al–Cu alloys [3–11]. Trace element or microalloying additions of Sn, Cd or In are well known to suppress low-temperature aging and enhance both the rate and extent of age hardening at elevated temperature, by promoting the formation of θ' at the expense of GP zones and θ'' [4,5]. Two types of proposal have been offered to describe the

* Corresponding authors.
 E-mail addresses: lgsammer@mail.xjtu.edu.cn (G. Liu), junsun@mail.xjtu.edu.cn (J. Sun).

mechanisms for this microalloying effect. One is that the Sn (Cd or In) atoms segregate to the precipitate/matrix interface and lower the interfacial energy somewhat [5–7]. This mechanism was first suggested [5] to account for the weak X-ray reflection observed during the early stages of aging, and subsequently received indirect experimental support separately from calorimetric measurements [6] and transmission electron microscopy (TEM) observations [7]. The other proposal is that the trace elements facilitate heterogeneous nucleation of θ', either directly at Sn (Cd or In)-rich particles [8] or indirectly at the dislocation loops present in the as-quenched microstructure [9]. In a later study using atom probe field ion microscopy [10], it was directly revealed that no Sn was segregated at the θ'/α-matrix interface in the Al–Cu alloys with trace Sn addition. Clusters of Sn atoms were detected in as-quenched samples, and the formation of Sn clusters was clearly found to precede the formation of θ'. These atom probe analyses indicated that heterogeneous nucleation of θ'; is the predominant microalloying mechanism in the Sn (Cd or In)-modified Al–Cu alloys. Similarly, the heterogeneous nucleation mechanism is also responsible for the recent findings [11,12] that minor additions of Si and Ge in Al–Cu increases hardness and produces a fast hardening rate when aged at elevated temperature, where the first formed Si–Ge precipitates provide preferential nucleation sites for metastable θ'' and then for θ' phases.

The addition of a minor amount of Mg in Al–Cu alloys, however, was found [13] to promote low-temperature aging, i.e. increasing the response on natural aging. The mechanism was suggested [13] to be that Mg atoms preferentially trap quench-in excess vacancies to retard Cu cluster formation in the initial aging stage. In the following aging stage, complex Cu/Mg/vacancy clusters are formed and act as effective nucleation sites for GP zones. The formation of Cu/Mg/vacancy complex clusters greatly retards the cluster growth and increases the cluster number density, accounting for the enhancement in the natural aging response.

Most recently, segregations of Si and Mg atoms at $\theta'/$ matrix interfaces have been visibly revealed in Al–Cu alloys with minor Si and Mg additions [14,15], by using the advanced three-dimensional atom probe tomography (3DAP). The solute atom segregation will change the interfacial conditions (e.g. interface structure, chemistry composition and energies) and cause a series of evolutions in both precipitation behaviors and strengthening responses, including precipitate nucleation and concomitantly number density and driving force for precipitate coarsening [16]. Solute segregation at precipitate/matrix interfaces is an important microalloying method to tailor the precipitation and improve the hardening response.

Previous investigations of the microalloying effect are mainly focused on the underlying mechanisms and hardening response. Little attention has been paid to the influence of minor microalloying elements on ductile fracture of Al alloys. As a type of structural material for technological applications, the Al alloys should have not only high strength but also excellent ductility. The addition of microalloying elements will inevitably affect the deformation capability and ductility of the Al alloys through changing the size, number density, distribution and even interfacial conditions of precipitates. On the one hand, the more homogeneous distribution of finer precipitates caused by the microalloying effect can relieve local stress/strain concentration during deformation and therefore increase the ductility. On the other hand, the presence of microalloying elements may lead to the deterioration in the ductility of Al alloys, such as by forming coarse constituent and additional other second phase particles [17,18], and/or by changing the precipitate/matrix interfacial conditions when segregating at the interfaces. Competition between these opposite effects will determine the deformation behaviors of the microalloyed Al alloys, which needs to be understood in order to aid the further design of advanced Al alloy.

In this paper, systematical studies were performed to investigate the effect of minor Sc addition on microstructural evolution, hardening response and especially ductile fracture of Al–Cu mode alloys. Al–Cu–Sc was chosen for the study because (i) our primary experimental results have shown [19] that the addition of trace amounts of Sc in Al–Cu alloys remarkably promotes the homogeneous precipitation of θ' and greatly reduces the precipitate size, displaying a significant microalloying effect; (ii) highly coarsening-resistant Al$_3$Sc particles (e.g. coarse primary Al$_3$Sc, intermediate Al$_3$Sc dispersoids and fine Al$_3$Sc precipitates; see Fig. 1) will be formed additionally [20], which can improve the high temperature performance of Al–Cu-based alloys and extend their applications; (iii) the binary Al–Cu alloys are a typical type of plate-like precipitate-containing aluminum alloys, which have attracted extensive theoretical studies on precipitation thermodynamics, kinetics and strengthening. They are also ideal mode materials for investigating the microalloying effect on ductile fracture.

2. Experimental procedures

2.1. Material preparation and heat treatments

Alloys with a composition of Al–2.5 wt.% Cu alloys (abbreviated Al–Cu alloys), Al–2.5 wt.% Cu–0.3 wt.% Sc (Al–Cu–Sc) and Al–0.3 wt.% Sc (Al–Sc) were respectively melted and cast in a stream argon, by using 99.99 wt.% pure Al, 99.99 wt.% pure Cu and mast Al–2.0 wt.% Sc alloy. The cast ingots were homogenized at 793 K for 24 h and hot extruded at 723 K into plates 14 mm in thickness and 60 mm in width. All the plates were subjected to the same heat treatments, i.e. solutionized at 863 K for 3 h, followed by a cold water quench and subsequently aged at 473 K, 523 K and 573 K, for a series of times. The maximum error of all the temperature measurements in the present experiments was ±1 K.
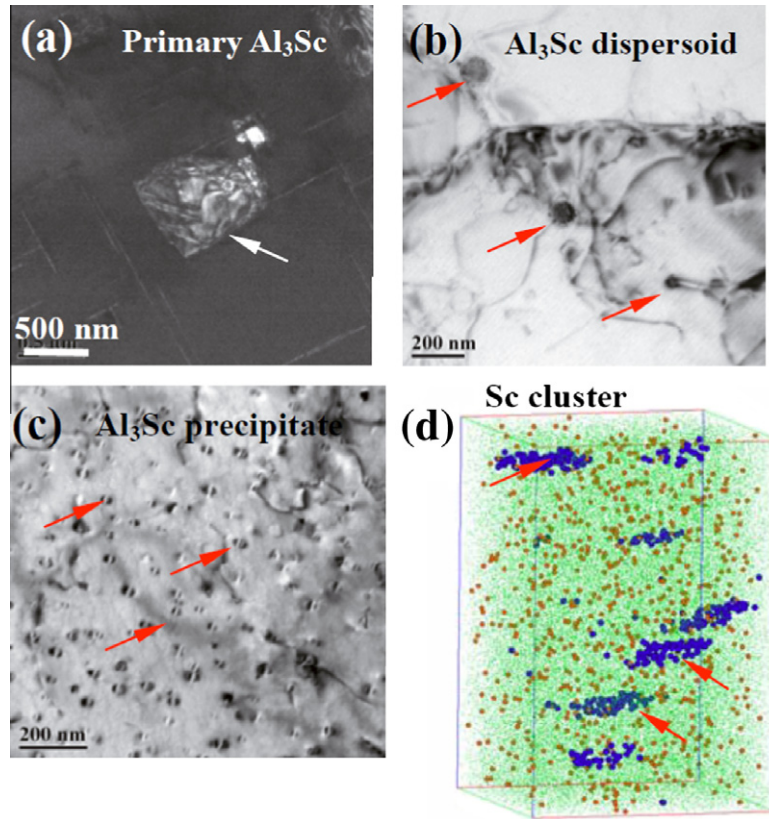
Fig. 1. Representative TEM images and 3DAP map showing multiscaled Sc-based particles and clusters (pointed by arrows) in present Al–Cu–Sc alloys, i.e. primary Al_3Sc particles in micrometer size (a), Al_3Sc dispersoids in sub-micro size (b), Al_3Sc precipitates in nanometer size (c) and Sc cluster in atomic level (d) (green = Al atoms, orange = Cu atoms, blue = Sc atoms, dimensions: $20 \times 20 \times 30$ nm). (For interpretation of the references to color in this figure legend, the reader is referred to the web version of this article.)

2.2. Microstructural characterizations

Microstructures of the alloys were characterized by using transmission electron microscopy (TEM) and high-resolution TEM. TEM foils were prepared following standard electro-polishing techniques for Al alloys. Quantitative measures of the number density and size of the precipitates were reported as average values of more than 200 measurements. Volume fraction of the second phase particles was determined by employing the corrected projection method [21,22], where the foil thickness of each captured region was obtained through convergent beam electron diffraction patterns [23]. Using the raw radius data of precipitates and the foil thickness in each area, the radius distributions were calculated after correction for the truncation effects based on a method by Crompton et al. [24]. Details about the measurements on precipitates, dispersoids and constituents are given in our previous publications [17,18,21,25].

In order to visibly reveal the microalloying mechanism at atomic level, 3DAP experiments were performed using an Imago Scientific Instruments 3000HR local electrode atom probe (LEAP). APT sample blanks with a square cross-sectional area of $\sim300 \times 300$ μm^2 and a 1 cm length were prepared by a combination of slicing and mechanical grinding. A two-step electropolishing procedure was used for making tips from these blanks [26,27]. A 10 vol.% perchloric acid in methanol solution was used for coarse polishing, and the final polishing was performed using a solution of 2 vol.% perchloric acid in butoxyethanol. APT data collection using the electrical pulsing mode was performed at a specimen temperature of 30 ± 0.3 K, with a voltage pulse fraction (pulse voltage/steady-state DC voltage) of 20%, a pulse repetition rate of 200 kHz and a background gauge pressure of $<6.7 \times 10^{-8}$ Pa (5×10^{-10} torr).

2.3. Measurements of mechanical properties

Tensile testing was used to measure yield strength (σ_0) and strain to fracture (ε_f) of the alloys. Smooth dog-bone-shaped tensile specimens have a gauge size of 6 mm in diameter and 30 mm in length, with their axis along the extrusion direction. The testing was performed at a constant strain rate of 5×10^{-4} s^{-1} with the load direction parallel to the specimen axis. The yield strength was determined as the 0.2% offset and the strain to fracture was determined as $\varepsilon_f = \ln(A_o/A_f)$, where A_o is the initial area and A_f is the area at fracture of the specimens.

3. Results

3.1. Microstructures of Al–Cu and Al–Cu–Sc alloys

Previous publications have reported that the addition of Sc in Al alloys may lead to the formation of primary Al_3Sc intermetallic phase [28,29] and Al_3Sc dispersoids [30,31], besides the Al_3Sc precipitates. In present work, both primary Al_3Sc (Fig. 1a) and Al_3Sc dispersoids (Fig. 1b) have been observed in the Al–Cu–Sc alloys. Quantitative measurements show that the primary Al_3Sc particles and Al_3Sc dispersoids have an average size of 0.6 μm and 50 nm, and a volume fraction of ~0.51% and 0.12%, respectively. The Al_3Sc dispersoids are especially effective in hindering the grain growth through Zener-drag action [30]. Besides, the presence of primary Al_3Sc can also refine the grains by promoting the heterogeneous grain nucleation [29]. These can well explain the present results that the as-quenched Al–Cu–Sc alloys have grains (in pancake shape with width of ~110 μm and length of ~800 μm) smaller than their Sc-free Al–Cu counterparts (width ~180 μm and length ~1300 μm). During the aging treatment, there is negligible change in the pre-existing microstructural characteristics of grains, primary Al_3Sc and Al_3Sc dispersoids, due to the relative low aging temperature. The apparent microstructural evolution is only the nucleation and growth of precipitates. Therefore, the aging-dependent strength and ductility are merely related to the precipitation, and the effect of grain size, primary Al_3Sc particles and Al_3Sc dispersoids, can be ignored.

Fig. 2 shows representative TEM images to demonstrate the size and distribution of θ' precipitates before and after Sc addition in the Al–Cu alloys, aged at three different tem-peratures for the same duration of 3 h, respectively. It can be visibly found that, at any aging temperature, the θ' precipitates in Al–Cu–Sc alloys always have a reduced size and increased number density compared with those in the Al–Cu alloys. This indicates that the Sc addition promotes the homogeneous precipitation of finer θ' in Al–Cu alloys, displaying a typical microalloying effect.

Statistical measurements on the radius (r_p) and thickness (h_p) of the plate-shaped θ' before and after Sc addition have been carefully conducted and the results are plotted in Fig. 3a–d as a function of aging time (t in s), respectively. It is quantitatively shown that (i) the Sc addition causes an ~20% decrease in both r_p and h_p when the aging temperature (T) is 473 and 573 K; (ii) the decrease can reach ~40–50% when T is 523 K; (iii) r_p and h_p in the $T = 523$ K Al–Cu–Sc alloys are close or even lower than those in the $T = 473$ K Al–Cu–Sc alloys. These hint that the microalloying effect of Sc addition is closely dependent on aging temperature and, among the three aging temperatures studied here, the most pronounced effect is reached at the intermediate temperature of $T = 523$ K. The reason for this extraordinary phenomenon will be proposed later when discussing the microalloying mechanisms.

The minor Sc addition in Al–Cu alloys can not only refine the θ' precipitates but also narrow the θ' size distribution to a large extent. This can be well illustrated by comparing the θ'-size distribution between the Sc-free and Sc-added Al–Cu alloys, as representatively shown in Fig. 3e vs. Fig. 3f at $T = 523$ K and $t = 3$ h. The θ'-size distribution is more concentrated in the Al–Cu–Sc alloys (Fig. 3f), indicative of more synchronous nucleation and growth of the θ' precipitates aided by the Sc atoms. However, the maximum volume
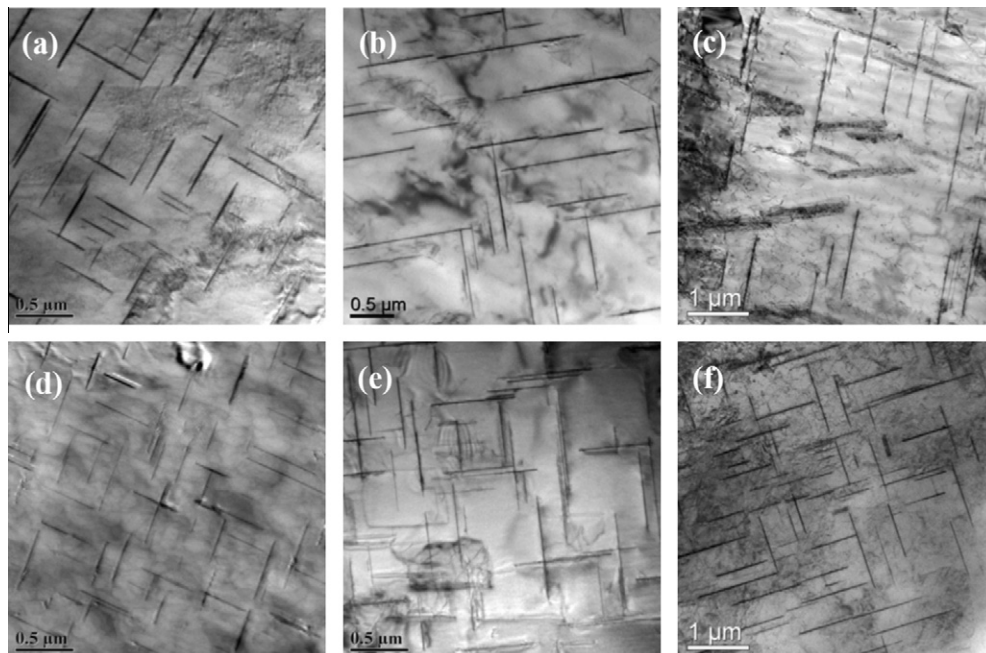

Fig. 2. Representative TEM images showing the size and distribution of θ' precipitates in the Al–Cu (a–c) and Al–Cu–Sc (d–f) alloys aged at 473 K (a and d), 523 K (b and e), and 573 K (c and f), respectively.
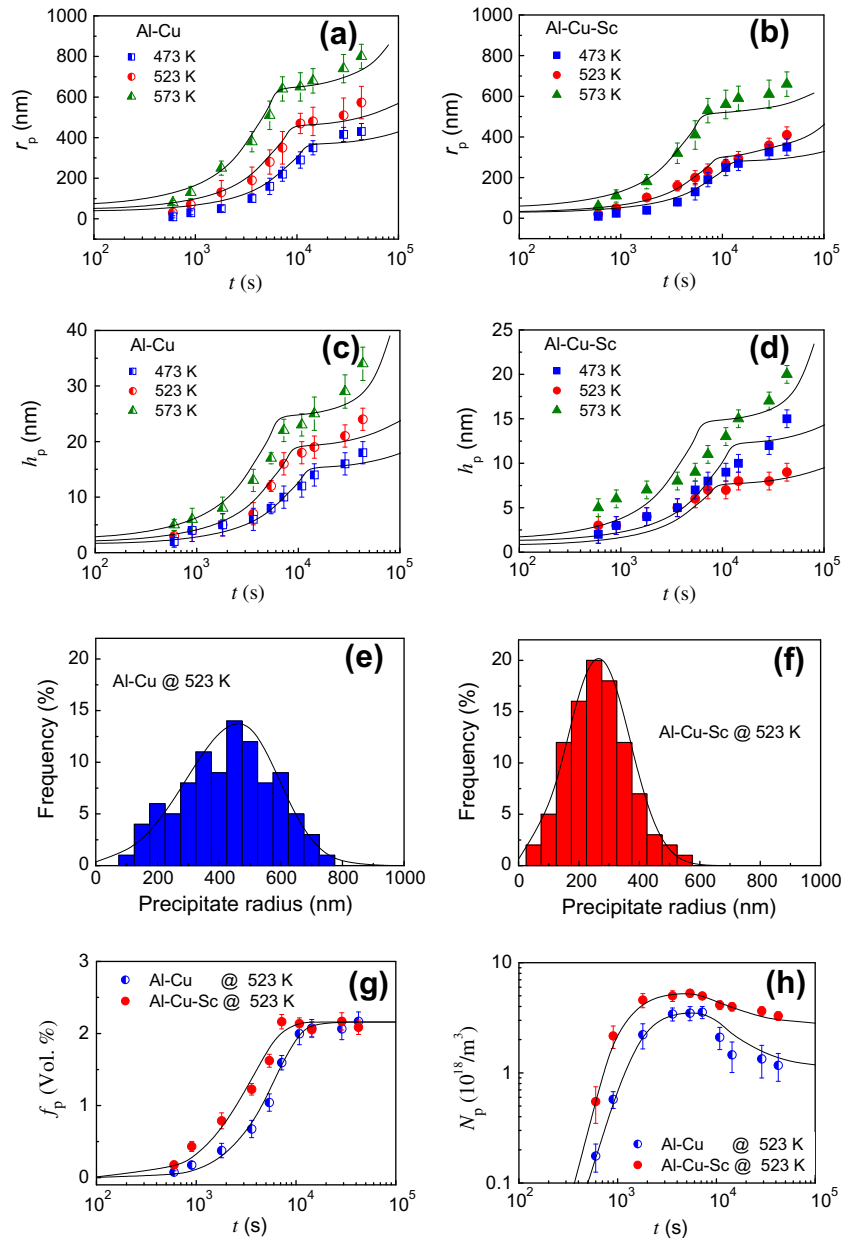
Fig. 3. Statistical results on the evolution of θ' precipitate radius (r_p) and thickness (h_p) with aging time (t) in Al–Cu (a and c) and Al–Cu–Sc (b and d) alloys aged at 473, 523 and 573 K, respectively. (e and f) are precipitate size distribution of Al–Cu and Al–Cu–Sc alloys aged at 523 K, respectively, for comparison. (g and h) are t-dependent precipitate volume fraction and number density of Al–Cu and Al–Cu–Sc alloys aged at 523 K, respectively.

fraction of θ' precipitates after peak aging is almost unchanged (Fig. 3g), which implies that the Sc addition has negligible influence on the saturated solution of Cu in Al matrix or on the excess Cu atoms available for θ' precipitation. The precipitation features characteristic of the Sc microalloying effect in the present alloys mainly include refined size (Fig. 3b and d), increased number density (Fig. 3h) and more uniform distribution (Fig. 3f).

Another issue of interest to note is that the thickness of θ' precipitates is retained to below 8 nm even when exposed to 523 K for 12 h. The high coarsening resistance of θ' precipitates was analyzed by using 3DAP examinations. Fig. 4 shows 3DAP element maps of the Al–Cu–Sc alloys aged at

523 K for 3 h. A θ' precipitate is just oblique cross the examined region, see the part assembled by Cu atoms (Fig. 4a–c). It seems that the Sc atoms roughly segregate at the θ'/matrix interfaces. To obtain 3DAP maps with higher spatial resolution and therefore to obtain more accurate data, local analyses were probed along the $[001]_\alpha$ direction, i.e. in the direction normal to the broad surface of the θ' plate. The cross-sectional element maps are shown in Fig. 5a–d. The corresponding composition profile is displayed in Fig. 5e. The solid vertical line in Fig. 5e indicates the location of the heterophase interface between the α-Al matrix and the θ' platelet, which is at the inflection point of the Al concentration profile. The
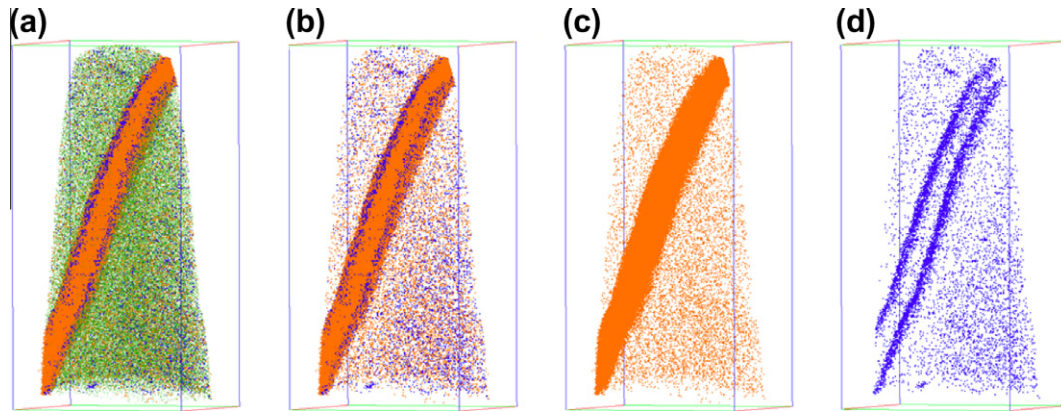
Fig. 4. 3DAP maps showing an oblique θ' precipitate and distribution of Al, Cu and Sc atoms in the Al–Cu–Sc sample aged at 523 K for 3 h (green = Al atoms, orange = Cu atoms, blue = Sc atoms, dimensions: 80 × 80 × 180 nm). Cu and Sc atoms are co-presented in (b), while only Cu atoms are presented in (c) and only Sc atoms in (d). Sc segregation at the θ'/matrix interfaces is visibly revealed. (For interpretation of the references to color in this figure legend, the reader is referred to the web version of this article.)
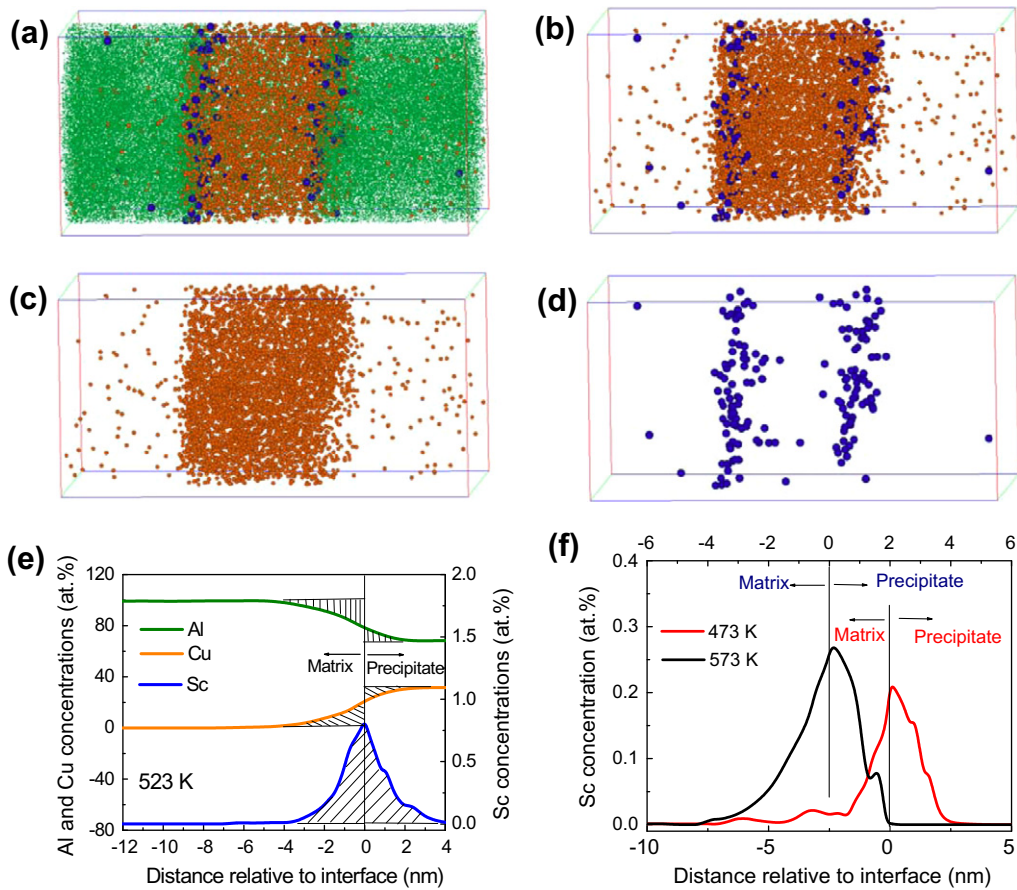

Fig. 5. 3DAP maps (a–d) typically showing distribution of Al, Cu, and Sc atoms across the θ'/matrix interface in the Al–Cu–Sc sample aged at 523 K for 3 h (green = Al atoms, orange = Cu atoms, blue = Sc atoms, dimensions: 20 × 20 × 40 nm). Cu and Sc atoms are co-presented in (b), while only Cu atoms are presented in (c) and only Sc atoms in (d). Sc segregation at the θ'/matrix interfaces is definitely verified. Corresponding proxigram is shown in (e), where the solid vertical line indicates the location of the heterophase interface between the θ' precipitate and matrix. (f) shows the proxigram of Sc cross the θ'/matrix interface in the Al–Cu–Sc sample aged at 473 and 573 K for 3 h, respectively. (For interpretation of the references to color in this figure legend, the reader is referred to the web version of this article.)

spatial concentration profiles of the θ' platelet and α-Al matrix are displayed on the right- and left-hand sides of this line, respectively. A high Sc concentration up to

0.8 at.% is shown at the interface, which is ~10 times greater than the Sc concentration within Al matrix (estimated to be ~0.08 at.% by subtracting the Sc atoms

consumed for forming primary Al_3Sc and Al_3Sc dispersoids). This provides evidence to verify the noticeable Sc aggregation at the broad face of the θ' precipitate. The θ' precipitates are well known [32] to possess a plate morphology with coherent interfaces to the α-Al matrix along its broad flat faces and semi-coherent interface at its periphery. Biswas et al. [15] have experimentally found that the Mg and Si segregation at the semi-coherent interface of θ' precipitate is a factor of two greater than at the coherent interface, showing a stronger segregation potential at the semi-coherent interface. Unfortunately in the present investigations, no 3DAP detections have been encountered at the semi-coherent interface, mainly due to the large size of θ' precipitates and hence the low probability of meeting the semi-coherent interface.

Orientated plate-like precipitates, such as θ' in Al–Cu-based alloys, have been generally believed to thicken by a ledge mechanism [33–35]. The overall thickening kinetics was commonly found to be somewhat slower than allowed by volume diffusion of the solute, which indicates an interface controlled mechanism. Since Sc atoms are segregated at the θ'/matrix interfaces, the motion of thickening ledge during the course of θ' growth must involve the simultaneous flux of Cu from the matrix to the riser of the ledge and the redistribution of Sc from the original broad face of the θ' plate to the terrace of the migrating thickening ledge. This is similar to the growing process of Ω phase in Al–Cu–Mg–Ag alloys [35,36]. The diffusion coefficient of Sc in Al matrix is $D_{Sc} = 1.9 \times 10^{-4} \exp(-164\ kJ\ mol^{-1}/RT)\ m^2\ s^{-1}$ [20], which is several orders less than that of Cu ($D_{Cu} = 4.4 \times 10^{-5} \exp(-134\ kJ\ mol^{-1}/RT)\ m^2\ s^{-1}$) within the studied temperature range. So the Sc aggregation at the θ'/matrix interfaces may limit the Cu atom diffusion and thus restrict the precipitate growth.

Similarly, the cross-sectional composition profile of θ' precipitate in the Al–Cu–Sc alloys aged at 473 and 573 K for 3 h has been respectively examined. Fig. 5f presents only the Sc concentration across the θ'/matrix interface. Sc aggregation at the interface is also clear in both the two samples. But the Sc concentration at interface is only ∼0.28 at.% (573 K) and ∼0.22 at.% (473 K), respectively, much less than that (∼0.80 at.%) in the 523 K-aged alloys. These atom-level findings seem to agree with the experimental measurements on precipitate sizes, considering Sc effect on inhibiting precipitate growth as mentioned above. The most Sc aggregation causes the most reduction in precipitate sizes in the 523 K-aged Al–Cu–Sc alloys, while reduction in both the 473 and 574 K-aged alloys is relatively less because the interfacial Sc aggregation and concomitant Sc inhibiting effect are weakened.

The most pronounced interfacial Sc segregation observed in the 523 K-aged Al–Cu–Sc alloys is possibly related to two requirements. One is that the Sc atoms should have enough diffusion capability to migrate towards the θ'/matrix interfaces. The other is that no Sc-based precipitates will be formed in order to ensure enough free Sc atoms available for interfacial segregation. The first

requirement can be achieved at relatively high aging temperature, while the second requirement needs a relatively low aging temperature because the Al_3Sc precipitates are ready to nucleate when the aging temperature is above ∼573 K [28]. Simultaneous meeting of the two opposite requirements results in an intermediate aging temperature where it becomes the most significant Sc segregation at θ'/matrix interfaces. This hypothesis can interpret the strongest interfacial Sc concentration in the 523 K-aged Al–Cu–Sc alloys rather than in the 473 and 573 K-aged alloys. In the next section, this hypothesis will be partially verified by the microstructural observations in Al–Sc alloys aged at the corresponding temperatures.

3.2. Microstructures of Al–Sc alloys

TEM and 3DAP examinations have been performed in the Al–Sc alloys aged at 473, 523, 573 and 673 K for 3 h. No precipitates have been found at $T = 473$ and 523 K. Fig. 6a and b shows representative 3DAP images of the 473 and 523 K-aged Al–Sc alloys, respectively. A large number of Sc clusters are clearly observed in the 523 K-aged alloy while only a small quantity of Sc clusters in the 473 K-aged alloy are observed. Since the cluster formation is controlled by the atom diffusion, it can be concluded that the diffusion of Sc atoms is considerably limited at the aging temperature of 473 K, consistent with above hypothesis. When T is raised to 573 K, Al_3Sc particles are precipitated (see Fig. 6c). These particles have a diameter ranging from 1.5 nm to 7 nm, with an average diameter of ∼3 nm. The average diameter of the Al_3Sc precipitates will increase to ∼7–8 nm at $T = 673$ K (Fig. 6d). Due to the abundant formation of Al_3Sc precipitates (e.g. number density of ∼$2 \times 10^{21}\ m^{-3}$ in the 573 K-aged alloy), Sc atoms remaining in the matrix are greatly reduced. This agrees with above hypothesis that Sc atoms available for interfacial segregation are limited once Sc-based precipitates formed.

3.3. Mechanical properties

Dependences of yield strength (σ_0) and fracture strain (ε_f) of Al–Cu and Al–Cu–Sc alloys on aging temperature T are shown in Fig. 7a–d, respectively, as a function of aging time t. Strength evolutions displayed in the present Al–Cu alloys are similar to previous reports [21,37] that the peak strength is slightly reduced while the time to peak-aging point is shortened with increasing T (Fig. 7a). The ductility is generally lowered at higher T (Fig. 7c) because larger precipitates formed at higher T are apt to induce local stress/strain concentration and hence cause early rupture [38].

In contrast, the evolutions in both strength and ductility become abnormal in the Sc-added Al–Cu alloys. The highest peak strength is found in the 523 K-aged Al–Cu–Sc alloy (Fig. 7b), which is increased by ∼30% and 50% in comparison with that of the 573 and 473 K-aged counterparts, respectively. Besides, the 523 K-aged Al–Cu–Sc alloy
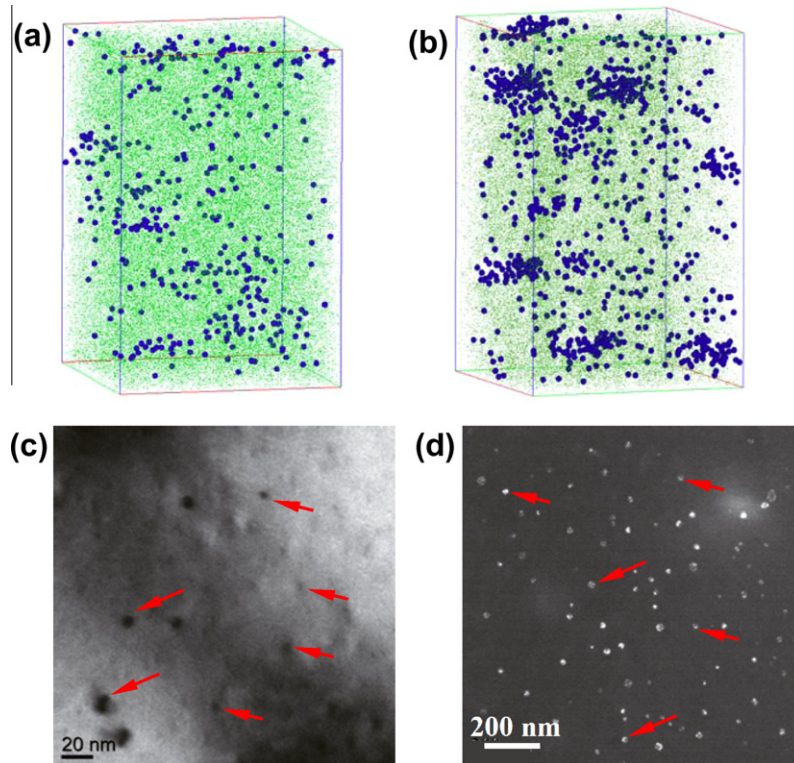
Fig. 6. 3DAP maps showing distribution of Al and Sc atoms in the Al–Sc alloys aged at 473 K (a) and 523 K (b) for 3 h (green = Al atoms, blue = Sc atoms, dimensions: 20 × 20 × 30 nm). (c and d) are typically TEM images showing the Al$_3$Sc precipitates in the Al–Sc alloys aged at 573 and 623 K for 3 h, as indicated by arrows. (For interpretation of the references to color in this figure legend, the reader is referred to the web version of this article.)

exhibits two extreme regions in the t vs. ε_f curve, i.e. the greatest ε_f when t is less than a critical point of $t_{cri} \approx 1.5$ h (or a critical precipitate radius of $r_p^{cri} \approx 200$ nm), with the lowest ε_f thereafter (Fig. 7d). There exists a sharp drop in ductility at the critical point, as marked in Fig. 7d. The 473 and 573 K-aged alloys, however, show a gradual decrease in ductility, radically different from what was observed in the 523 K-aged alloys.

It is easy to explain why the highest peak-aging strength is observed in the 523 K-aged Al–Cu–Sc alloy, because microstructural examinations have disclosed the most reduction in precipitate sizes and simultaneously the most promotion in precipitate density in this alloy caused by the most pronounced Sc effect. The refined precipitates are generally believed [17,18,39,40] to reduce the deformation discrepancy between the matrix and the precipitates, which will alleviate the local stress/strain concentration and hence enhance the ductility. This can interpret the greatest ductility in the first regime of $r_p < r_p^{cri}$, but cannot explain the lowest ductility in the second regime of $r_p > r_p^{cri}$. The sharp decrease in ductility observed at r_p^{cri} indicates a size-dependent transition in fracture mechanisms.

In situ TEM tensile testing was further performed on the $T = 523$ K and $t = 3$ h Al–Cu–Sc alloy in order to reveal the fracture mechanism in the $r_p > r_p^{cri}$ regime. Fig. 8a captures a crack at the rim of the TEM sample that is vertical to the direction of applied tensile stress. Two orthogonal variants of θ' precipitates are dispersed ahead of the crack

tip. One variant of the precipitates is approximately parallel with the crack (defined P-type precipitates), while the other is almost vertical to the crack. Applying tensile stress progressively, interfacial decohesion was observed at the P-type precipitates ahead of the crack tip, as typically shown in a magnified TEM image in Fig. 8b. Interfacial decohesion triggers interfacial microcracks, which will truncate primary crack growth, preclude large accumulations of strain and result in low ductility. Fig. 8c and d shows representative TEM images indicating how the crack propagates along some matrix/precipitate interfaces, creating orthogonal growth segments coincident well with the precipitate orientations. In contrast, no interfacial decohesion and resultant crack propagation along the matrix/precipitate interfaces have been observed in the $T = 523$ K and $t = 1$ h Al–Cu–Sc alloy (within the $r_p < r_p^{cri}$ regime) when subjected to the same in situ TEM tensile testing. This hints that interfacial decohesion at the matrix/precipitate interface is responsible for the low ductility at the regime of $r_p > r_p^{cri}$ or $t > t_{cri}$. A micromechanical model will be developed in Section 4 to address the fracture behavior caused by the interfacial decohesion and analyze the critical condition for interfacial decohesion.

One may wonder whether the Sc clusters or Al$_3$Sc precipitates should have predominant effect on the ductile fracture of the Al–Cu–Sc alloys, since the solute clusters [41–43] and Al$_3$Sc particles [44–46] have been revealed to interact with dislocations substantially and therefore affect
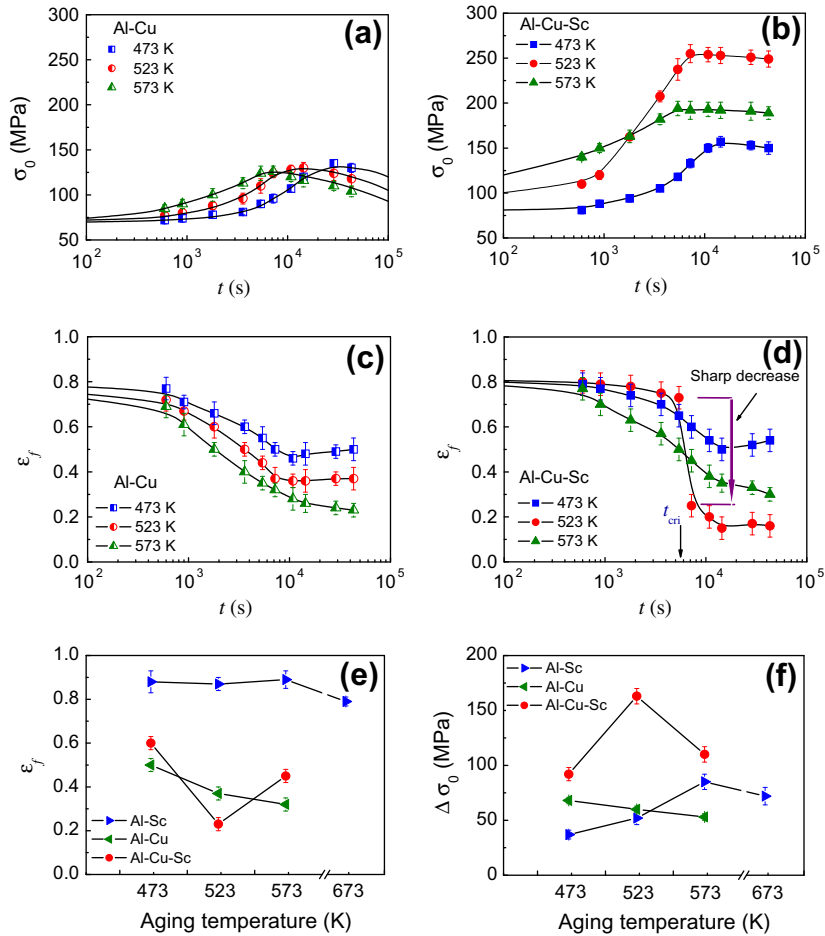
Fig. 7. Dependence of yield strength (σ_0) (a and b) and the strain to fracture (ε_f) (c and d) of Al–Cu (a and c) and Al–Cu–Sc alloys on aging temperature (T) as a function of aging time (t). T-dependent ε_f (e) and precipitation strength increment ($\Delta\sigma_0 = \sigma_0 - \sigma_0^i$, where σ_0^i is the initial yield strength before aging treatment) (f) of the Al–Cu, Al–Cu–Sc and Al–Sc alloys for comparison (t = 3 h).

the strengthening response as well as deformation behaviors. However, our experimental measurements on pure Al–Sc alloys show that there is no apparent change in the ductility among the Al–Sc alloys peak-aged at 473, 523 and 573 K, respectively (see Fig. 7e). A perceptible decrease in the ductility can be only detected at T = 673 K. This clearly indicates that neither the Sc clusters nor the fine Al$_3$Sc precipitates predominantly affect the ductile fracture of the present Al–Cu–Sc alloys. It is the θ'-related local deformation behaviors, including deformation incompatibility and interfacial decohesion, that play a key role in the ductile fracture process and be responsible for the abnormal sharp decrease in ductility in the 523 K-aged Al–Cu–Sc alloy.

Fig. 7f displays the yield strength increment ($\Delta\sigma_0 = \sigma_0 - \sigma_0^i$, where σ_0^i is the initial yield strength before aging treatment) induced by age-hardening in Al–Cu, Al–Sc, and Al–Cu–Sc alloys aged at different T for 3 h, respectively. The maximum $\Delta\sigma_0|_{Al-Cu-Sc}$ in the Al–Cu–Sc alloys occurs at 523 K, while the maximum $\Delta\sigma_0|_{Al-Sc}$ in the pure Al–Sc alloys comes at T = 573 K. This discrepancy hints that the strengthening effect in the present Al–Cu–Sc alloys is not

predominantly contributed by Sc clusters or Al$_3$Sc precipitates. It is because a large number of Sc atoms have been segregated at the θ'/matrix interfaces in the Al–Cu–Sc alloys, and Sc clusters or Al$_3$Sc precipitates therein are remarkably reduced by compared with their Al–Sc counterparts (see the statistical results in Table 1). The high $\Delta\sigma_0|_{Al-Cu-Sc}$ in the Al–Cu–Sc alloys is then believed to be mainly related to the θ'-strengthening effect, given the significant reduction in θ' size and promotion in θ' density especially at T = 523 K.

4. Discussion

In the above section, we have presented experimental results that Sc atoms are prone to segregate at the θ'/matrix interfaces, which modifies the θ' nucleation/growth and impacts on the strengthening response and fracture behaviors. The Sc segregation effect exhibits a nonmonotonic aging temperature-dependence, resulting in the maximum strengthening effect at T = 523 K while an unexpected low ductility is due to interfacial decohesion. In this section, reduction in θ'/matrix interfacial free energy will be quantitatively evaluated by taking into account the interfacial Sc
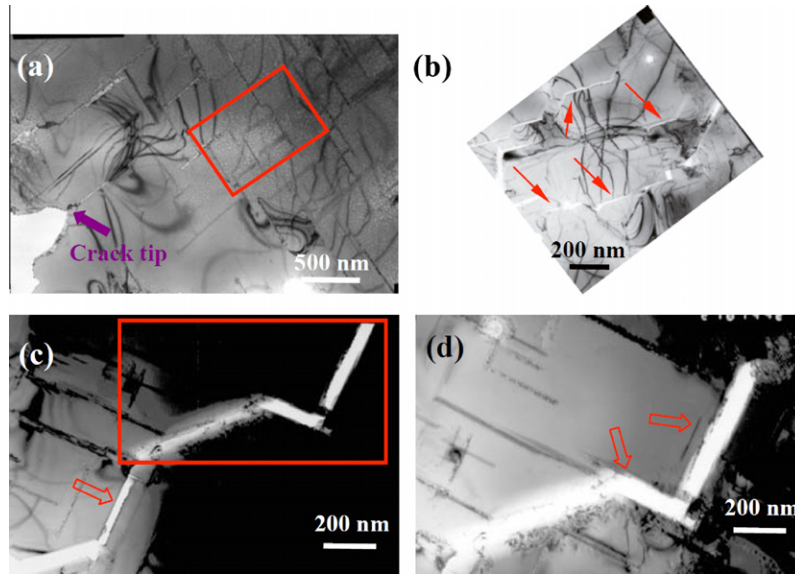
Fig. 8. Representative images captured during in-site TEM tensile testing to show crack propagation aided by interfacial decohesion at θ'/matrix interfaces in the Al–Cu–Sc alloy aged at 523 K for 3 h. (a) shows a crack and the θ' precipitate distribution ahead of the crack tip before testing. After applying external stress to some extent, some θ' precipitates ahead of the crack tip will suffer from interfacial decohesion. A magnified TEM image on the region corresponding to the boxed part in (a) is displayed in (b) to visibly demonstrate the interfacial decohesion (indicated by closed arrows) and concomitantly the formation of interfacial voids. Further increasing the applied stress, the main crack will propagate along the interfacial voids. (c and d) are representative images displaying the crack propagation along the matrix/precipitate interfaces and the creation of some orthogonal growth segments (indicated by open arrows) that are coincident well with the precipitate distribution. (d) is a magnified image of the region boxed in (c). Compared with (c), contrast is re-adjusted in (d) to show the θ' plates and their distribution more clearly.

Table 1
Statistical results on the parameters of Sc clusters and Al$_3$Sc precipitates in Al–Cu–Sc and Al–Sc alloys.

Alloys	T (K) ($t = 3$ h)	Sc clusters[+]	Al$_3$Sc precipitate	
		Number density (10^{22} m^{-3})	Size (nm)	Number density (10^{21} m^{-3})
Al–Cu–Sc	473	0.35 ± 0.13	–	–
	523	1.22 ± 0.45	–	–
	573	–	4.1 ± 1.5	0.82 ± 0.31
Al–Sc	473	0.74 ± 0.23	–	–
	523	4.16 ± 0.51	–	–
	573	–	3.5 ± 2.2	2.04 ± 0.22

[+] The minimum cluster size is $N_{min} = 10$, the maximum separation distance $d_{max} = 0.5$ nm.

segregation, which will be used to interpret the observed strengthening effect on the basis of the maximum precipitate growth rate hypothesis [47,48]. In addition, a micromechanical model will be developed to rationalize the abnormal ductile fracture caused by the size-dependent interfacial decohesion in the 523 K-aged Al–Cu–Sc alloys.

4.1. Reduction in interfacial free energy caused by interfacial Sc segregation

Si segregation at θ'/α-Al matrix interfaces and Mg segregation at Al$_3$Sc/α-Al matrix interfaces have been demonstrated by Seidman's group [14,15,49,50] using atom probe tomography. They also proposed a thermodynamic method for quantitative analyses of interfacial segregation of solute atoms across heterophase interfaces. Here, we adopt their analytical method to quantitatively assess the

reduction in interfacial free energy caused by the Sc segregation at the θ'/α-Al matrix interfaces.

Following their treatments, the relative Gibbsian interfacial excess is firstly determined to provide a quantitative thermodynamic evaluation for Sc segregation in the ternary Al–Cu–Sc alloys [51]:

$$\Gamma_{Sc}^{rel} = \Gamma_{Sc} - \Gamma_{Cu} \frac{c_{Al}^{\alpha} c_{Sc}^{\theta'} - c_{Al}^{\theta'} c_{Sc}^{\alpha}}{c_{Al}^{\alpha} c_{Cu}^{\theta'} - c_{Al}^{\theta'} c_{Cu}^{\alpha}} - \Gamma_{Al} \frac{c_{Sc}^{\alpha} c_{Cu}^{\theta'} - c_{Sc}^{\theta'} c_{Cu}^{\alpha}}{c_{Al}^{\alpha} c_{Cu}^{\theta'} - c_{Al}^{\theta'} c_{Cu}^{\alpha}} \quad (1)$$

where Γ_{Sc}^{rel} is the Gibbsian interfacial excess of Sc relative to Cu and Al; Γ_{Sc}, Γ_{Al} and Γ_{Cu} are the Gibbsian interfacial excess of Sc, Al and Cu, respectively; and c_i^{α} and $c_i^{\theta'}$ are the concentrations of an element ($i = $ Al, Cu or Sc) in the α-Al matrix and θ' precipitates. Referring to a representative proxigram as shown in Fig. 5e, the shaded areas in the proxigram represent the individual Γ_i [14] and the

values of Γ_i are determined using proxigram concentration profiles from

$$\Gamma_i = \rho \Delta x \sum_{m=1}^{q} \left(c_i^m - c_i^k \right) \qquad (2)$$

where ρ is the atomic density, Δx is the distance between the q concentration data points in the proxigram, c_i^k is the concentration of an element i at each data point and $k = \alpha$ on the α-Al matrix side and $k = \theta'$ on the precipitate side of the heterophase interface.

From the Gibbs adsorption isotherm for a system with two phase and $n \geqslant 3$ components [52], a coefficient for the reduction of interfacial free energy (γ) at a concentration c_i due to segregation of component i at the heterophase interface, assuming a dilute solution model, is given by [49,50,53,54]:

$$\left. \frac{\partial \gamma}{\partial c_i} \right|_{T,P,\mu_1,\ldots,\mu_{i-1},\mu_{i+1},\ldots,\mu_n} = -k_B T \frac{\Gamma_i^{cri}}{c_i} \qquad (3)$$

where Henry's law for dilute solution is assumed, μ_i is the chemical potential of component i, k_B is Boltzmann's constant and T is the absolute temperature. As to the interfacial Sc segregation in the present Al–Cu–Sc alloys, the reduction in γ due to the interfacial Sc solute excess can be calculated by evaluating the following integral [55]:

$$-\frac{1}{k_B T \Gamma_{Sc}^{rel}} \int_{\gamma_{initial}}^{\gamma_{final}} d\gamma = \int_{c_{Sc}^{initial}}^{c_{Sc}^{final}} \frac{dc_{Sc}}{c_{Sc}} \qquad (4)$$

Here $c_{Sc}^{initial}$ and c_{Sc}^{final} are the Sc concentration in the α-Al matrix and the peak concentration of Sc at the θ'/α-Al matrix interface, respectively.

Using the 3DAP experimental data on concentrations, the reduction in interfacial free energy ($\Delta\gamma$) caused by Sc segregation at the θ'/α-Al matrix interfaces can be quantitatively evaluated from Eqs. (1)–(4). The determined $\Delta\gamma$ are $\sim$−13.1, −42.3 and −17.6 mJ m^{-2} for the Al–Cu–Sc alloys aged at 473, 523 and 573 K for 3 h, respectively, as listed in Table 2. Note that the plate-like θ' precipitates have coherent interface (CI) to the α-Al matrix along their broad flat faces and semi-coherent interface (SCI) at their periphery. As mentioned before, we merely captured the 3DAP images/data for the coherent interfaces (see Fig. 5) and failed to access to the semi-coherent interfaces, due to large radius of the θ' precipitate and small areal fraction of the semi-coherent interface. The $\Delta\gamma$ quantitatively determined here is that for the coherent interfaces $\Delta\gamma_{CI}$. Biswas et al. [15] have made first attempt to quantitatively assess the difference between CI solute segregation and SCI solute segregation at the θ' precipitate, and found that the $\Delta\gamma$ for

the SCI is approximately five times greater than that for the CI. Simply, we will used a scaling factor κ to estimate the reduction in SCI interfacial energy, i.e. $\Delta\gamma_{SCI} = \kappa \Delta\gamma_{CI}$.

Previous atomic simulations on θ' precipitate in Al–Cu alloys [32] have given the interfacial free energy of $\gamma_{CI} = 170$ mJ m^{-2} for the CI and $\gamma_{SCI} = 520$ mJ m^{-2} for the SCI. Refer to $\Delta\gamma_{CI} = -42$ mJ m^{-2} evaluated for the 523 K-aged Al–Cu–Sc alloy, it is striking to find a $\sim$25% reduction in the interfacial energy caused by the interfacial Sc segregation. Kirchheim's thermodynamic calculations [56] have clearly demonstrated that solute segregation at grain boundary, by decreasing the grain boundary energy, can reduce the grain size of polycrystalline materials and take advantage of the hardening effect of grain boundaries. The inhibition of grain growth is mainly related to the reduction in driving force for grain coarsening (a result of decreased grain boundary energy) rather than the solute drag effect [56]. Similarly, theoretical predictions [57,58] also revealed that excess solute at the precipitate/matrix interface can stabilize the size of precipitates. These calculations support our present experimental results that precipitate size is reduced when Sc is added and segregated at the precipitate/matrix interface, especially in the 523 K-aged Al–Cu–Sc alloy where the strongest interfacial Sc segregation or the most decrease in interfacial energy is accompanied by the most pronounced reduction in precipitate size. Since the deformation behaviors of heat-treatable Al alloys is closely dependent on the precipitate size and distribution that are in turn controlled by the interfacial energy, the variation in interfacial energy caused by interfacial Sc segregation will have a marked impact on the strengthening effect and fracture mechanism, as discussed below.

4.2. Effect of interfacial Sc aggregation on strengthening effect

Experimental results have revealed that the strengthening effect in present Al–Cu–Sc is predominantly contributed by the θ' precipitates. Some models have been proposed [21,59–63] to quantitatively describe the strengthening effect of plate-like precipitate. The interparticle spacing λ_p between the plate-like precipitates, which is usually related to the size (r_p), volume fraction (f_p) and number density (N_f) of the precipitates, is believed to be the key factor in precipitation strengthening. Although precipitation strengthening is also strongly impacted by the heterophase interfaces between the matrix and precipitates, the effect of heterophase interfaces has been barely taken into account in these models. The reason is that the character of heterophase interfaces is hard to be characterized in a quantitative way. In this paper, by using the advanced 3DAP and adopting the analytical method proposed by Seidman's group, we have quantified the changes in interfacial energy under different interfacial Sc segregation. It is then possible to make an attempt to correlate the interface energy to mechanical properties simply but directly.

Table 2
Summary of the calculations on $\Delta\gamma$ caused by interfacial Sc segregation in the Al–Cu–Sc alloys.

T (K)	473	523	573
$\Delta\gamma$ (mJ m^{-2})	−13.1 ± 2.5	−42.3 ± 3.4	−17.6 ± 1.8

Extensive studies on the diffusional growth of plate-like precipitates have shown that the precipitate lengthening rate is constant in time [33,64] prior to soft impingement of adjacent neighbor precipitates (soft impingement is schematically illustrated in Fig. 9a). The Zener–Hillert expression for the lengthening rate is given by [47,48,65]:

$$\frac{dr_p}{dt} = \frac{D_{Cu}}{2 \cdot R_p} \frac{c_{Cu}^{\alpha} - c_{Cu}^{\theta'/\alpha}}{c_{Cu}^{\theta'} - c_{Cu}^{\theta'/\alpha}} \left(1 - \frac{R_c}{R_p}\right) \qquad (5)$$

where D_{Cu} is the Cu solute diffusivity, $c_{Cu}^{\theta'/\alpha}$ is the Cu concentration in the matrix at the precipitate/matrix growing interface, R_p is the radius of the plate tip and R_c is the plate tip radius at which growth would stop because capillary effects reduce the driving force for Cu diffusion to zero [47,48]. According to Zener [48], the radius of the diffusion zone around the plate tip (R_{dz}, see Fig. 9a) is proportional to the plate tip radius R_p. Hillert [47] found that the proportionality between R_{dz} and R_p is ~2, i.e. $R_{dz} = 2R_p$. Zener further proposed a maximum growth rate hypothesis [48] that the stable plate lengthening conditions will only prevail for values of R_p close to that yielding the maximum growth rate. The maximum growth rate is achieved for $R_p = 2R_c$ [47,48]. The critical plate tip radius R_c is, in turn, a function of interfacial energy of the plate tip γ_{SCI} and the onset driving force ΔG_v as $R_c \setminus \gamma_{SCI}/\Delta G_v$ [66]. Therefore, the interparticle spacing between adjacent precipitates can be expressed in terms of γ_{SCI} and ΔG_v:

$$\lambda_p = 2R_{dz} = 2 \cdot (2R_p) = 2 \cdot (2 \cdot (2R_c)) = \frac{8L\gamma_{SCI}}{\Delta G_v} \qquad (6)$$

where L is a constant to reflect the homogeneity of precipitate size and dimensional distribution. In the case of perfectly monotonic precipitate size distribution and perfectly random site distribution, L is expected to be close to 1 and λ_p has the minimum value of λ_p^{min} [61]. In reality, however, not all precipitate plate tips will impinge on another plate at exactly the same time. As demonstrated in Fig. 9a, although several plates have reached the condition of soft impingement, several other have not yet. This will cause L to be greater than 1 and $\lambda_p > \lambda_p^{min}$. The value of L captures this effect and is expected to increase with the width of the precipitate size distribution [61].
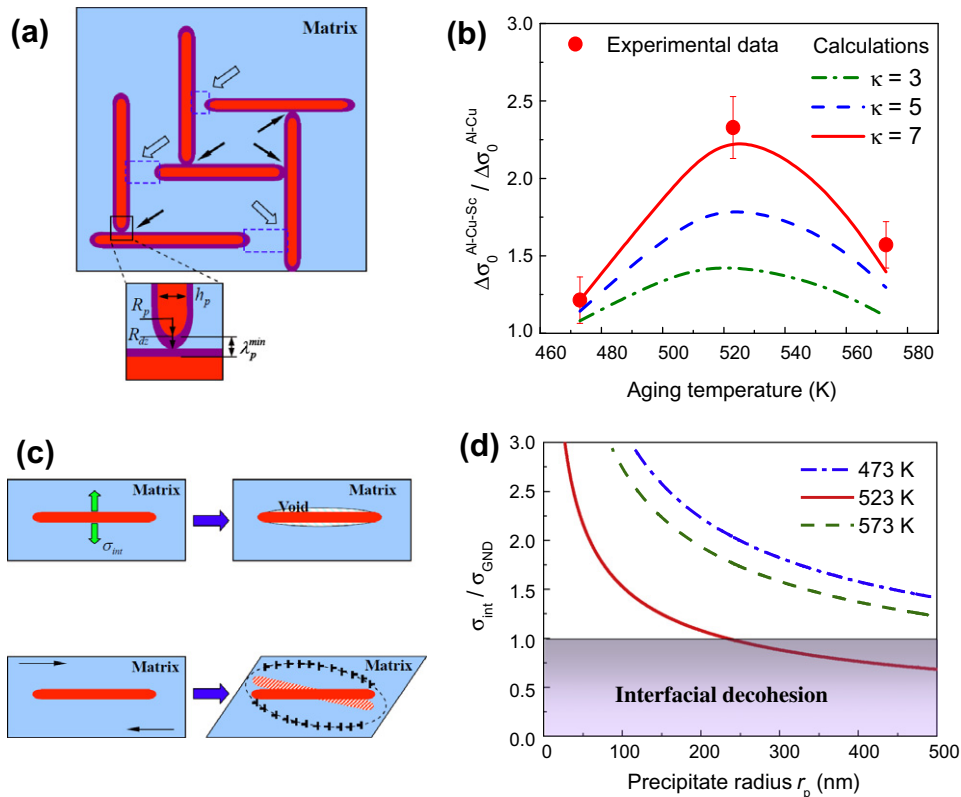

Fig. 9. (a) Sketch illustrating soft impingement of adjacent θ' plates (indicated by solid arrows) and definition of parameters of R_p, R_{dz}, and λ_p^{min}. Red plates represent θ' precipitates, purple surrounding represents solute diffusion field, and blue background represents the Al matrix. Note that some plates do not reach soft impingement, as indicated by open arrows. (b) Calculations on normalized $\Delta\sigma_0^{Al-Cu-Sc}/\Delta\sigma_0^{Al-Cu}$ as a function of aging temperature, in comparison with experimental results. (c) Sketches illustrating interfacial decohesion and concomitantly interface void formation at the θ'/matrix interfaces under a critical stress σ_{int} (the upper one), and the generation of geometrically necessary dislocations (GNDs) to accommodate the deformation incompatibility between θ' precipitate and Al matrix (the bottom one). (d) Calculation of $\sigma_{int}/\sigma_{GNDs}$ as a function of precipitate radius r_p. $\sigma_{int}/\sigma_{GNDs} < 1$ means that the local stress caused by GNDs will exceed σ_{int} and hence induce interfacial decohesion. Otherwise, interfacial decohesion hardly occurs and the matrix Al will be finally rupture due to the excess storage of GNDs. (For interpretation of the references to color in this figure legend, the reader is referred to the web version of this article.)

Substituting Eq. (6) into the Orowan equation leads directly to a relationship between the precipitation strengthening and the precipitate/matrix interfacial energy:

$$\Delta\sigma_0 \propto \Delta\tau \propto \frac{\mu b}{\lambda_p} \propto \frac{\mu b \Delta G_v}{8 L \gamma_{SCI}} \qquad (7)$$

where μ is the shear modulus of the matrix and b is the Burgers vector. Simply assuming that L and ΔG_v are constant and insensitive to the change in γ_{SCI}, the above equation can show the dependence of precipitation strengthening increment on the reduction in γ_{SCI} caused by interfacial Sc segregation. Normalizing the peak-aged $\Delta\sigma_0$ of Al–Cu–Sc alloys by that of their Sc-free counterparts, some unknown parameters can be divided out and a reduced expression will be obtained as:

$$\left.\frac{\Delta\sigma_0^{Al-Cu-Sc}}{\Delta\sigma_0^{Al-Cu}}\right|_T = \left.\frac{\gamma_{SCI} + \Delta\gamma_{SCI}}{\gamma_{SCI}}\right|_T \qquad (8)$$

The subscript T in the above equation represents the aging temperature. Using the values of $\Delta\gamma_{SCI}$ determined before, the normalized $\Delta\sigma_0$ can be calculated as a function of aging temperature or $\Delta\gamma_{SCI}$. Calculations are in broad agreement with the experimental results, referring to the comparison in Fig. 9b.

At this point, it should be specially mentioned that the strengthening response is directly determined by the precipitate size, content and distribution. The influence of interfacial energy on strengthening response is actually implemented by affecting the precipitation. The derivation of Eq. (8) is aimed at correlating the strengthening response with the interfacial energy (characterizing the degree of interfacial solute segregation) in an intuitive and semiquantitative manner, which may be helpful for theory-assisted alloy design of new microalloyed Al alloys with high performance.

4.3. Effect of interfacial Sc segregation on the size-dependent fracture mechanism

Interfacial decohesion has been experimentally revealed in the Al–Cu–Sc alloy aged at 523 K for a prolonged time, which is responsible for the sharp reduction in ductility. The nucleation of cavities at the particle/matrix interface caused by plastic deformation has been studied numerous times and some criteria have been proposed, see Ref. [67] by Goods and Brown and references therein. Any energy-based model, including the critical stress and the critical strain ones, should consider the effect of interface energy of the particle/matrix interfaces, because the interfacial decohesion involves the creation of new surfaces of matrix material and particles, as well as the disappearance of particle/matrix interface. Sun [68] has developed an interfacial decohesion model to derive the critical stress (σ_{int}) required for void initiation at the interface, where the energy balance condition was obtained by applying the concept of energy release rate in linear elastic fracture mechanics.

The interfacial decohesion strengths obtained from this model fit well with those measured experimentally in spheroidized steels that contain sub-micron-sized particles [68]. The present θ' precipitates have a radius at the same sub-micron level; we extend Sun's model to account for the interfacial decohesion at the plate-like θ' precipitates (Fig. 9c), which yields an expression for the interfacial stress σ_{int} as

$$\sigma_{int} = \sqrt{\left(\frac{E_m + E_p}{2}\right)\frac{\pi\gamma_{total}}{r_p(1-v^2)}} \qquad (9)$$

where $E_m = 70$ GPa [25] and $E_p = 180$ GPa [69] are the elastic moduli of the matrix and the θ' precipitate, respectively; $v = 0.3$ is Poisson's ratio; and γ_{total} is the total change in surface/interfacial energy caused by interfacial decohesion, i.e.

$$\gamma_{total} = \gamma_{Al}^{sur} + \gamma_{\theta'}^{sur} - \gamma_{CI} \qquad (10)$$

Here γ_{Al}^{sur} and $\gamma_{\theta'}^{sur}$ are the surface free energy of Al and θ' that have values of ~1.0 and ~2.5 J m^{-2} [70], respectively. Eqs. (9) and (10) show that σ_{int} varies inversely with both precipitate size r_p and θ'/matrix interfacial energy γ_{CI}. This means that the plate-like θ' precipitates with greater size and/or higher interfacial energy are more apt to suffer interfacial decohesion under plastic deformation.

However, the trigger of interfacial decohesion requires that the local stress reaches σ_{int}. Generally, the local stress under plastic deformation consists mainly of applied external stress, hydrostatic tensile stress and local flow stress that is induced by the geometrically necessary dislocations [67]. Due to the deformation incompatibility between the Al matrix and θ' precipitate, gradients of deformation form and geometrically necessary dislocations (GNDs) are induced to accommodate the deformation gradients [71,72]. The density of GNDs (ρ_{GND}) is closely dependent on the interparticle spacing λ_p between the θ' precipitates [25,72]:

$$\rho_{GND} = \frac{\varepsilon_{local}}{4b\lambda_p} \qquad (11)$$

where ε_{local} is the local shear strain and the expression for λ_p has been given in Eq. (6). The local flow stress caused by GNDs is then given by

$$\sigma_{GND} = \eta\mu b(\rho_{GND})^{1/2} = \eta\mu\left(\frac{b\varepsilon_{local}\Delta G_v}{32 L \gamma_{SCI}}\right)^{1/2} \qquad (12)$$

where η is a constant of order of 1. Since Al alloys have relatively lower strength (or lower applied stress), the local stress is predominantly contributed by σ_{GND}, especially when λ_p is nano-size as in the present work. We can simply define the criterion for interfacial decohesion of θ' precipitate as:

$$\sigma_{GND} \geqslant \sigma_{int}, \quad \text{or} \quad \sigma_{int}/\sigma_{GND} \leqslant 1 \qquad (13)$$

Eqs. (12) and (13) reveal that the lower the value of γ_{SCI}, the greater is σ_{GND}. This means that interfacial decohesion
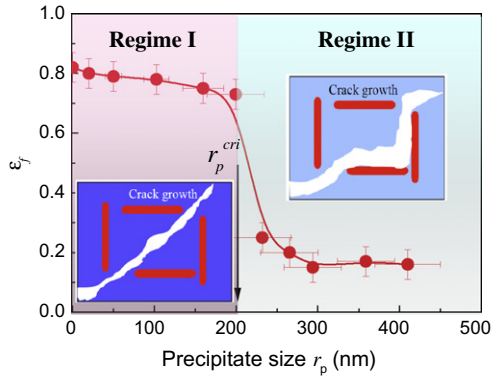
Fig. 10. Precipitate size-dependent fracture mechanism map of the Al–Cu–Sc alloy aged at 523 K. Two regimes, I and II, are divided by a critical size of $r_p^{cri} \sim 200$ nm. In regime II, interfacial decohesion at the θ'/matrix interfaces is ready to happen and the fracture mechanism is crack propagation aided by interfacial voids (right insert). In regime I, local stress is not enough to trigger the interfacial voiding and the fracture mechanism is predominantly matrix Al rupture (left insert). Note that the matrix undergoes more intense plastic deformation in the case of I, which results in higher ductility. The dark blue color in the background of the left insert indicates more intense deformation compared with the light blue color of the right insert. (For interpretation of the references to color in this figure legend, the reader is referred to the web version of this article.)

is most possible to happen in the 523 K-aged Al–Cu–Sc alloy, because the most pronounced interfacial Sc segregation in this alloy causes the most reduction in γ_{SCI}. In addition, interfacial decohesion is more likely to occur in the case of greater precipitate size, as mentioned before.

For quantitative reasons, $\sigma_{int}/\sigma_{GND}$ is calculated as a function of precipitate size r_p for the Al–Cu–Sc alloys aged at 473, 523 and 573 K, respectively. Some values of parameters [17,21] for calculations include $\mu = 28$ GPa, $b = 0.286$ nm, the maxim $\varepsilon_{local} \sim 0.4$ and $\Delta G_v \sim 100$ kJ mol^{-1} that was previously determined in Al–Cu alloys [73]. The calculations are shown in Fig. 9d. $\sigma_{int}/\sigma_{GND} < 1$ is found in the 523 K-aged Al–Cu–Sc alloy when r_p is greater than ~ 200 nm, indicative of interfacial decohesion thereafter. While in the 473 and 573 K-aged Al–Cu–Sc alloys, $\sigma_{int}/\sigma_{GND}$ is constantly larger than 1, which indicates that the crack propagation is mainly through matrix fracture rather than interfacial decohesion in the two alloys. These calculations are consistent with the experimental results.

The interfacial Sc segregation is now proven to have a dual effect on the ductile fracture of Al–Cu–Sc alloys. On the one hand, the reduction in interfacial energy caused by the Sc segregation increases the critical interfacial stress, which prevents the interfacial decohesion. On the other hand, narrower distribution of θ' precipitates with finer size is induced by the interfacial Sc segregation, which produces more GNDs around the precipitates and as a result greater local stress under applied loading. A competition thus exists between the two contrary effects, which is tailored by both the interfacial energy and the precipitate size. When the local stress is greater than the critical interfacial

stress in the conditions of lower interfacial energy and longer precipitate size, the fracture mechanism is interfacial decohesion-aided crack growth that results in low ductility. Otherwise, the fracture mechanism is predominantly Al matrix rupture, accompanied with high ductility. The transition in fracture mechanisms is just observed in the 523 K-aged Al–Cu–Sc alloy. Fig. 10 shows the size-dependent fracture mechanism map in this alloy. The critical size $r_p^{cri} \sim 200$ nm divides the map into two regimes, I and II, which display different deformation behaviors and fracture mechanisms.

5. Conclusions

(1) Sc segregation at the θ'/matrix interfaces has been characterized by using 3DAP. This interfacial solute segregation, limiting the precipitate growth and promoting the precipitate nucleation, results in narrow distribution of θ' precipitates with reduced sizes.

(2) Interfacial Sc segregation in 523 K-aged Al–Cu–Sc alloy is more pronounced than in both 473 and 573 K-aged alloys. This is related to the two requirements for interfacial solute segregation, i.e. enough Sc diffusion rate and available free Sc atoms, which can be met in the 523 K-aged alloy but only partially met in the two other temperature aged alloys.

(3) Reduction in interfacial energy caused by Sc segregation has been evaluated quantitatively and the 523 K-aged Al–Cu–Sc alloy has the greatest reduction in interfacial energy. This can well interpret the highest strength observed in the 523 K-aged alloy, based on the relationship between precipitation strengthening and interfacial energy.

(4) A sharp decrease in ductility has been found in the 523 K-aged Al–Cu–Sc alloy at a critical precipitate size of ~ 200 nm. This was experimentally found to be caused by the interfacial decohesion at the θ'/matrix interfaces ahead of the main crack. A micromechanical model, taking into account the effect of both interfacial energy and precipitate size, has been developed to rationalize the interfacial decohesion that is related to the interfacial Sc segregation.

References

[1] Hornbogen E, Starke Jr EA. Acta Metall 1993;41:1.
[2] Martin JW. Precipitation hardening. 2nd ed. Boston (MA): Butterworth-Heinemann; 1998.
[3] Ringer SP, Hono K. Mater Charact 2000;44:101.
[4] Hardy HK. J Inst Met 1952;80:483.
[5] Silcock JM, Heal TJ, Hardy HK. J Inst Met 1955;84:23.
[6] Boyd JD, Nicholson RB. Acta Metall 1971;19:1101.
[7] Sankaren R, Laird C. Mater Sci Eng 1974;14:271.
[8] Kanno M, Suzuki H, Kanoh O. J Jpn Inst Met 1980;44:1139.
[9] Van Nuyten JBM. Acta Metall 1967;15:1765.
[10] Ringer SP, Hono K, Sakurai T. Metall Mater Trans 1995;26A:2207.
[11] Mitlin D, Radmilovic V, Dahmen U, Morris Jr JW. Metall Mater Trans 2001;32A:197.
[12] Mitlin D, Radmilovic V, Morris Jr JW, Dahmen U. Metall Mater Trans 2003;34A:735.
[13] Sato T, Hirosawa S, Hirose K, Maeguchi T. Metall Mater Trans 2003;34A:2745.
[14] Biswas A, Siegel D, Wolverton C, Seidman DN. Acta Mater 2011;59:6187.
[15] Biswas A, Siegel D, Seidman DN. Phys Rev Lett 2010;105:076102.
[16] Strudel JL. In: Chan RW, Haasen P, editors. Physical metallurgy, vol. 2. Amsterdam: North-Holland; 1983.
[17] Liu G, Sun J, Nan CW, Chen KH. Acta Mater 2005;53:3459.
[18] Liu G, Zhang GJ, Wang RH, Hu W, Sun J, Chen KH. Acta Mater 2007;55:273.
[19] Chen BA, Pan L, Wang RH, Liu G, Cheng PM, Xiao L, et al. Mater Sci Eng A 2011;A530:607.
[20] Marquis EA, Seidman DN. Acta Mater 2001;49:1909.
[21] Liu G, Zhang GJ, Ding XD, Sun J, Chen KH. Mater Sci Eng 2003;A344:113.
[22] Gilmore DL, Starke Jr EA. Metall Mater Trans 1997;28A:1399.
[23] Kelly PM, Jostens A, Blake RG, Naiper JG. Phys Status Solidi (a) 1975;31:771.
[24] Crompton JMG, Waghorne RW, Broke GB. Br J Appl Phys 1966;17:1301.
[25] Liu G, Zhang GJ, Ding XD, Sun J, Chen KH. Metall Mater Trans 2004;35A:1725.
[26] Miller MK. Atom probe tomography: analysis at the atomic level. New York: Kluwer Academic/Plenum Publishers; 1999.
[27] Krakauer BW, Seidman DN. Rev Sci Instrum 1992;63:4071.
[28] Røyset J, Ryum N. Inter Mater Rev 2005;50:19.
[29] Norman AF, Prangnell PB, McEwen RS. Acta Mater 1998;46:5715.
[30] Jones MJ, Humphreys FJ. Acta Mater 2003;51:2149.
[31] Ferry M, Burhan N. Acta Mater 2007;55:3479.
[32] Vaithyanathan V, Wolverton C, Chen LQ. Acta Mater 2004;52:2973.
[33] Aaronson HI, Laird C. Trans AIME 1968;242:1437.
[34] Sankaran R, Laird C. Acta Metall 1974;22:957.
[35] Reich L, Murayama M, Hono K. Acta Mater 1998;46:6053.
[36] Hutchinson CR, Fan X, Pennycook SJ, Shiflet GJ. Acta Mater 2001;49:2827.
[37] Hardy HK. J Inst Met 1951;79:321.
[38] Hahn GT, Rosenfield AR. Metall Trans A 1975;6:653.
[39] Garrett GG, Knott JF. Metall Trans A 1978;9:1187.
[40] Staley JT. Aluminum 1979;55:277.
[41] Marceau RKW, Sha G, Ferragut R, Dupasquier A, Ringer SP. Acta Mater 2010;58:4923.
[42] Ringer SP, Hono K, Sakurai T, Polmear IJ. Scripta Mater 1997;36:517.
[43] Starink MJ, Wang SC. Acta Mater 2009;57:2376.
[44] Seidman DN, Marquis EA, Dunand DC. Acta Mater 2002;50:4021.
[45] Fazeli F, Poole WJ, Sinclair CW. Acta Mater 2008;56:1909.
[46] Nieh TG, Hsiung LM, Wadsworth J, Kaibyshev R. Acta Mater 1998;46:2789.
[47] Hillert M. Jernkont Ann 1957;141:757.
[48] Zener C. Trans AIME 1946;167:550.
[49] Marquis EA, Seidman DN, Asta M, Woodward C, Ozolins V. Phys Rev Lett 2003;91:036101.
[50] Marquis EA, Seidman DN, Asta M, Woodward C. Acta Mater 2006;54:119.
[51] Dregia SA, Wynblatt P. Acta Metall Mater 1991;39:771.
[52] Defay R, Prigogine I, Bellemans A, Everett DH. Surface tension and adsorption. New York: Wiley; 1966. p. 89.
[53] Isheim DI, Gagliano MS, Fine ME, Seidman DN. Acta Mater 2006;54:841.
[54] Seidman DN, Krakauer BW, Udler D. J Phys Chem Solids 1994;55:1035.
[55] Krug ME, Dunand DC, Seidman DN. Acta Mater 2011;59:1700.
[56] Kirchheim R. Acta Mater 2002;50:413.
[57] Kirchheim R. Acta Mater 2007;55:5129.
[58] Kirchheim R. Acta Mater 2007;55:5139.
[59] Kelly PM. Scripta Metall 1972;6:647.
[60] Zhu AW, Starke Jr EA. Acta Mater 1999;47:3263.
[61] da Costa Teixeira J, Cram DG, Bourgeois L, Bastow TJ, Hill AJ, Hutchinson CR. Acta Mater 2008;56:6109.
[62] Nie JF, Muddle BC, Polmear IJ. Mater Sci Forum 1996;217–222:1257.
[63] Nie JF, Muddle BC. J Phase Equilib 1998;19:543.
[64] Fennante M, Doherty RD. Scripta Metall 1976;10:1059.
[65] Hillert M, Hoglund L, Agren J. Acta Mater 2003;51:2089.
[66] Hillert M. In: Aaronson HI, editor. Lecture on the theory of phase transformation. Warrendale (PA): TMS; 1999.
[67] Goods SH, Brown LM. Acta Metall 1979;27:1.
[68] Sun J. Int J Fract 1990;44:R51.
[69] Eshelman FR, Smith JF. J Appl Phys 1978;49:3284.
[70] Zhang JM, Ma F, Xu KW. Appl Surf Sci 2004;229:34.
[71] Ashby MF. Philos Mag 1970;21:399.
[72] Brown LM, Stobbs WM. Philos Mag 1976;34:351.
[73] Liu G. Ph.D. thesis, Xi'an Jiaotong University; 2002.